

# The Feasibility of Detecting Supercooled Liquid with a Forward-Looking Radiometer

Ian S. Adams *Member, IEEE*, and Justin Bobak *Member, IEEE*

**Abstract**—Icing due to supercooled liquid poses a threat to manned and unmanned aircraft. Particularly with the proliferation of unmanned systems, light-weight passive sensors could allow remote detection of supercooled liquid. A three-dimensional radiative transfer model is utilized to determine the feasibility of a forward-viewing passive sensor for remotely detecting hazardous icing conditions. An analysis of simulated passive microwave spectra for a forward-viewing passive sensor finds dependencies on the liquid water content, cloud distance, and temperature, and sensitivity is noted across the millimeter-wave spectrum. Spectral flattening in the shoulders of molecular resonances corresponds to the presence of clouds, while saturated brightness temperatures near the transition lines are linked to the ambient temperature. A principal component analysis shows significant information content at G band near the water vapor molecular transition, suggesting compact radiometer systems to detect and range supercooled liquid are feasible. Additional information content may be available at K<sub>a</sub>-band, suggesting such observations would be useful when size and mass are not constrained.

**Index Terms**—Millimeter wave radiometry, clouds

## I. INTRODUCTION

Supercooled liquid water exists in the atmosphere as cloud droplets down to temperatures of  $-40^\circ$  and are an important component of the global radiation budget [1]. These droplets present in mixed-phase clouds pose a hazard to aviation through airframe icing. From 1999 to 2007, there were 62 in-flight icing reports, with approximately half of the incidents resulting in fatalities [2]. Early research efforts into nose or pod mounted sensors produced promising results; however, no such systems have been operationally integrated into aircraft. The advent of remotely-piloted and autonomous aircraft has renewed interest in developing remote sensors for detecting supercooled liquid, due to the lack of human environmental awareness in unmanned aerial systems. Moreover, the expanded use of G-band radiometry, both due to the reduced component size and proximity to the 183.1-GHz water vapor line [3], suggest that a small system for detecting, and even coarsely ranging, supercooled liquid clouds may be possible. Such systems with limited size, weight and power consumption would be ideal for unmanned aerial systems.

Simulating the response to horizontally-finite clouds adds additional complexity to radiative transfer calculations. To address the icing detector issue, the Air Force Geophysics Laboratory's RADTRAN radiative transfer model was modified to have a concentric-layered atmosphere [4]. While the

model was not capable of including scattering ice species for horizontal views, it showed an appreciable response to liquid water droplets at 37 GHz. Simulations at 89 GHz showed a far more muted response to horizontal views, and other frequencies were not considered, nor were finite antenna patterns.

In the present work, we use the Atmospheric Radiative Transfer Simulator (ARTS) [5] to simulate the response to a horizontally-finite mixed-phase cloud. The three-dimensional capabilities ARTS allow for horizontally-finite clouds and finite antenna beams. Monte Carlo integration is used to solve the radiative transfer equation in three-dimensions in a scattering environment. A simple cloud model is created, based on observations of Arctic mixed-phase clouds, to demonstrate the spectral response to variations in liquid water content and temperature, and the line-of-sight distance to the cloud is also considered. The Arctic case was chosen due to the significance of supercooled liquid to the modulation of sea ice, as well as the anticipation of increased Naval operations in the Arctic as sea ice recedes in a warming climate. The ability for both environmental observing and military unmanned systems to avoid hazardous icing conditions is desirable for both civilian and defense agencies. Simulations demonstrate the feasibility of a G-band sensor for detecting supercooled liquid clouds, with notable dependence on the amount of liquid water as well as the range to the observed cloud. Additional sensitivity to the local ambient temperature is noted. Section II provides an overview of the cloud scenario used in the simulation, and the simulation tools. Section III provides the results of the simulations, while the discussion and concluding remarks are presented in Section IV.

## II. MODELING OVERVIEW

### A. Atmospheric Scenario

To determine the passive microwave response to clouds at horizontal viewing angles, we constructed a simplified cloud model based on observations of mixed-phase clouds [6]. The profile of liquid, pristine ice, and aggregated snow is shown in Fig. 1. A gamma distribution is used to represent all hydrometeor species:

$$n(r) = \frac{3 \times 10^{18} w}{4\pi\rho\beta^4\Gamma(\gamma+3)} \left(\frac{r}{\beta}\right)^{\gamma-1} e^{-\frac{r}{\beta}} \quad (1)$$

where  $r$  is the particle radius in  $\mu\text{m}$ ,  $W$  is the water content in  $\text{g m}^{-3}$ ,  $\rho$  is the density of liquid or ice water in  $\text{g m}^{-3}$ ,  $\gamma$  is a dimensionless shape parameter, and  $\beta = r_e/(\gamma+2)$ . The effective radius  $r_e$  is the ratio of the third moment of the size distribution to the second. Finally, the number density at each

I. S. Adams is with Mesoscale Atmospheric Processes Laboratory, NASA Goddard Space Flight Center, Greenbelt, MD, 20771 USA. He was previously with the Remote Sensing Division, Naval Research Laboratory. e-mail: ian.s.adams@nasa.gov

J. Bobak is with the Remote Sensing Division, U. S. Naval Research Laboratory, Washington, DC, 20375 USA.

radius  $n(r)$  has units of  $\mu\text{m m}^{-3}$ . In this form, changes to water content simply scale the size distribution. The prescribed values of  $r_e$  used in this study for liquid cloud, pristine ice, and aggregated snow are  $10 \mu\text{m}$ ,  $20 \mu\text{m}$ , and  $100 \mu\text{m}$ , respectively, and for the shape parameter we use  $\gamma = 3$ . The pristine ice crystals are assumed to have planar geometries, based on the growth regime consistent with the temperature within and directly below the liquid layer [7]. For analyzing the response to variation in liquid water, the liquid water profiles are scaled such that the profile peak has values of 0.1, 0.2, 0.4, and  $0.8 \text{ g m}^{-3}$ .

The temperature, pressure, diatomic oxygen ( $\text{O}_2$ ), diatomic nitrogen ( $\text{N}_2$ ), water vapor ( $\text{H}_2\text{O}$ ), ozone ( $\text{O}_3$ ) profiles are taken from the Air Force Geophysics Laboratory Atmospheric Constituent Profiles [8] database included with the ARTS supplementary data, specifically the zonal-mean profiles for subarctic winter. The temperature and derived relative humidity profile, which are german to the results presented in Section III, are given in Fig. 2. The water vapor profile has been converted from volume mixing ratio to relative humidity:

$$RH = VMR \frac{p}{e_s} \times 100\% \quad (2)$$

where  $p$  is pressure and  $e_s$  is the saturation vapor pressure [9] over water, both in Pa. The relative humidities at the bottom of the column are adjusted so that the layers in which clouds are present are near saturation with respect to liquid. For input into the radiative transfer model, the humidity profile is then converted back into volume mixing ratio based on the shifted temperature profile, where the entire temperature profile is shifted by 0, 6, and 12 K. When the temperature profile is shifted, the pressure profile is adjusted such that the ratio of pressure to temperature remains constant.

The model atmosphere varies vertically, but is horizontally homogeneous. The one exception is that, since the three-dimensional nature of the radiative transfer model allows for horizontally-finite clouds, the cloud extends 111.3 km (or  $1^\circ$  longitude on a spherical Earth model) along the sensor flight direction and 556.6 km perpendicular to the flight direction. The spatial dimensions of the cloud are consistent with observed Arctic clouds: shallow in vertical extent, but extended horizontally. Such clouds persist, on average, for 12 hours but can have lifetimes of many days [10].

### B. Radiative Transfer Description

To perform radiative transfer simulations, we used the Atmospheric Radiative Transfer Simulator (ARTS), version 2.3 [5]. For the purposes of simulating radiances in a three-dimensional atmosphere, we utilize the reverse Monte Carlo integration, which can also account for multiple scattering effects [11]. The reverse Monte Carlo algorithm relies on importance sampling to handle the non-diagonal extinction matrices inherent with horizontally aligned particles. This model has been used to simulate brightness temperatures for space-based sensors for both limb [12] and conical [13] geometries, producing synthetic radiances that are consistent with observations. It has also compared well with other models for ground-based geometries [14]. While the simulation

horizontal geometries is relatively novel, the performance of the model for other geometries gives us confidence for using the model in the present study.

Hydrometeor scattering properties for ice particles are calculated using the T-Matrix method for fixed orientation [15] with a temperature-dependent complex permittivity for ice [16]. Pristine ice particles are represented with cylindrical plates of solid ice with a 4:1 aspect ratio, and aggregates are oblate spheroids with an aspect ratio of 1.33:1 and a density of  $0.2 \text{ g cm}^{-3}$ . The effective permittivity is calculated using the Maxwell-Garnett mixing formula for elliptical inclusions [17], with a lattice of ice containing inclusions of air. While T-Matrix calculations are not as representative as the higher-fidelity discrete dipole approximation [18] for frozen hydrometeors with irregular shape, a comprehensive database of DDA-computed particles is not available for preferentially-aligned snow particles with random azimuthal orientation. Moreover, pristine particles of small sizes, such as those at the location of the liquid layer, can be modeled well using idealized but representative geometries [19].

The von Mises distribution [20], which is a good directional statistics approximation of a Gaussian distribution, is used to characterize particle flutter. Defined over a semi-circle,

$$p(\theta) = \frac{e^{\kappa \cos(2(\theta-\mu))}}{\pi I_0(\kappa)}. \quad (3)$$

The parameters  $\mu$  and  $\kappa$  give the mean and spread of the distribution, with  $\kappa$  being inversely proportional to standard deviation. For the frozen hydrometeors, flutter is defined with a spread parameter of seven, (Gaussian-equivalent standard deviation of approximately  $11^\circ$ ).

Supercooled cloud liquid droplets are modeled as a spherical scattering species using the T-Matrix for random orientations [21] with complex permittivity prescribed by Turner et al. [22]. Gas absorption for  $\text{N}_2$ ,  $\text{O}_2$  and  $\text{H}_2\text{O}$  is calculated using the complete Rosenkranz absorption model [23], [24], [25], with improvements to  $\text{O}_2$  absorption [26]. Absorption for  $\text{O}_3$  is calculated using line data from the HITRAN catalog [27]. While the contribution of  $\text{O}_3$  is expected to be minimal, as the volume mixing ratios in the troposphere are two orders of magnitude below the upper atmosphere peak, ozone is included for completeness, and the inclusion of  $\text{O}_3$  requires negligible computing resources.

### III. SIMULATION RESULTS

In the simulations, the sensor is placed at an altitude of 1.35 km, which corresponds to the peak in the liquid water content, and we prescribe a half-power beamwidth of  $1^\circ$  at all frequencies (30 to 200 GHz). The spectrum is sampled at 2-GHz intervals. The Monte Carlo standard error is set to 0.2 K; however, there are some points at high optical depth that converge rapidly but get stuck at the saturation temperature. While the Monte Carlo error for the  $I$  component of the Stokes vector for these points is below the standard error threshold, the error in  $Q$  (polarization difference) remains high. Future modifications to the Monte Carlo integration will take the convergence of  $Q$  into account. To remove these anomalous points, spectra are processed with a three-element median

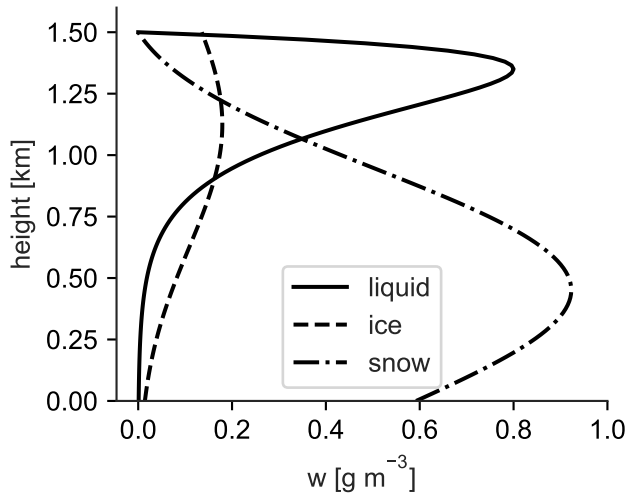


Fig. 1. Cloud profile showing liquid water and two frozen hydrometeor species.

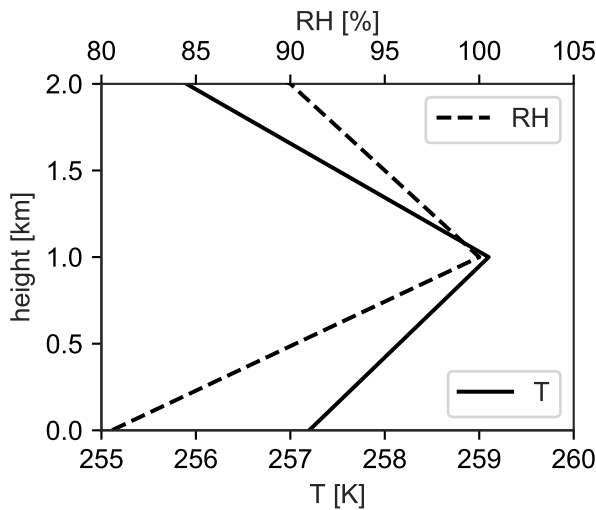


Fig. 2. AFGL subarctic winter temperature profile and modified humidity profile.

filter, but some artifacts can remain at the edges of spectral line features or when consecutive frequencies are saturated. The ice water content is not varied in the present work, and the peak amount of ice is extreme for Arctic mixed-phase clouds. However, simulations comparing icy and no-ice scenarios differ by no more than 1 K.

*A. Varying Liquid Water Content*

Placing the sensor 25.6 km from the cloud edge, we look at the dependence on liquid water content. The resulting spectra are shown with solid lines in the top panel of Fig. 3, and the clear sky spectrum is given for reference. The response is fairly monotonic with increasing liquid for window regions

TABLE I  
SENSOR GEOMETRY

Distance (km)	Displacement (m)	Diameter (m)
0.00	0.00	0.00
7.79	4.76	136
16.7	21.8	292
25.6	51.4	447
33.4	87.4	583

of the spectra. Near molecular resonances (60 GHz and 118 GHz for O<sub>2</sub> and 183.31 for H<sub>2</sub>O), the spectra are saturated at a temperature below the local ambient temperature of 258 K. For the 60 GHz O<sub>2</sub> complex, the brightness temperature saturates at 256.6 K for all cloud conditions, including no cloud. At 118 GHz, there a one Kelvin variation between 254 (clear sky) and 255 K (saturated), with the brightness temperature quickly saturating with increasing cloud. This is not surprising as this spectral feature is weaker than the 60 GHz oxygen complex. The brightness temperatures are saturated at 253.6 K at the 183.31 GHz water vapor line. Compared with the remote (25.6 km) view of the cloud, the spectra are much more compressed when the sensor is located 7.8 km from the cloud edge (dashed line). There is some difference in compression for the different window regions (30-50 GHz versus 75-110 GHz versus 130-170 GHz). Below 50 GHz, there is still considerable variation in the spectra over the range of liquid water content. In the middle window region, there is still some dependence to liquid water content, but the spectra eventually saturate at the highest water content values. In the highest window region, the spectra quickly saturate; although, there is some variation for lower amounts of liquid water.

Highlighting the spectral response near the H<sub>2</sub>O molecular transition at 183.1 GHz, in Fig. 4 we see significant spectral flattening with increasing liquid water content and decreasing distance to the cloud edge. Looking at the differential brightness temperatures between the line peak (183.1 GHz) and 170 GHz, the clear sky case is about 13.7 K. For 0.8 g m<sup>-3</sup> at 25.6 km, this compresses to 8.7 K, and for the same amount liquid water, but only 7.8 km from the cloud, it is 0 K.

*B. Varying Distance*

A similar exercise is performed fixing the liquid water content at 0.1 g m<sup>-3</sup>, and varying the sensor location. Table I shows the line-of-sight distance between the sensor and the cloud edge along the sensor boresight, along with the vertical displacement from the liquid peak at the cloud pierce point. For the distances given, the line-of-sight distance deviates from the arc distance by less than 10 m at the farthest point. Additionally, diameter of the projected beam at the half-power level is given to show that the increase in vertical displacement with distance is a fraction of the beam diameter. The boresight of the antenna is shifted less than one sixth of the half-power beamwidth at the farthest distance, but there is increased smoothing of the brightness temperature contribution from the liquid layer with distance.

As with the liquid water dependence, the sensor response to changing distance is monotonic in window regions and saturated at the molecular resonances, as shown center panel of Fig. 3 (solid lines), with the saturation temperatures matching those from the simulations of varying liquid. Above the 60-GHz  $O_2$  lines, the spectral flattening with decreasing distance is similar to the spectral flattening with increasing water content; however, at the lower frequencies (below 50 GHz) the spectral flattening is not quite as strong as the liquid water response. When the liquid water is increased to  $0.4 \text{ g m}^{-3}$  (dashed lines), there is additional flattening of the spectra, and the middle and upper window regions become saturated.

### C. Shifting Temperature Profile

The third free parameter we investigate is temperature, looking at clear sky simulations (solid), and simulations where the liquid water content was set to  $0.4 \text{ g m}^{-3}$  (dashed). The sensor is located 16.7 km from the cloud edge. These simulation results are shown in the bottom panel of Fig. 3. Near the molecular transitions where the spectra saturate, the shifts in the temperature profiles result in equal shifts of the spectra. For the window regions, the behavior is much more complex due to the commensurate changes in water vapor. By holding the relative humidity constant while the temperature is increased, the  $H_2O$  volume mixing ratio is increased by a factor of 2.5 to 2.6 in the region of interest for a 12-K temperature shift.

### D. Dimensionality Reduction

Principal component analysis (PCA) is typically applied to reduce the dimensionality of high-dimensional systems. While the free parameters that we investigate comprise an artificially low dimensional system, additional parameters (namely pressure and  $H_2O$ ) change with shifts to the temperature profile. Hence, we use PCA elucidate the information content of the performed simulations. In performing this analysis we are ignoring the inherent non-linearities and non-Gaussian behavior of the simulated system. The variations in liquid water, distance, and temperature are those listed previously.

Figure 5 shows a scatter plot of the first two principal components, with the colormap corresponding to frequency. There is an obvious separation in behavior between the low frequencies (below 50 GHz) and the high frequencies. Frequencies near the molecular transitions have low scores in the first principal component, which reflects the saturation with respect to liquid water content and distance. The W-band window region spans a similar, albeit wider, range of scores in the first principal component, compared with the G-band window region, suggesting both some level of redundancy along with slightly increased sensitivity at W band.

The three window regions are stratified with respect to the second principal component, with the window region between 70 and 110 GHz having the lowest scores. Notably, both the portion of the G-band spectrum near the  $H_2O$  line, as well as  $K_a$ -band frequencies exhibit appreciable scores in both principal components, while also populating very different regimes in principal component space, suggesting that these

two regions of the millimeter wave spectrum contain unique and complementary information.

## IV. CONCLUSIONS

The simulations demonstrate that liquid cloud layers can be detected using a forward looking radiometer, and that the spectral response to the cloud depends both on distance and liquid water content. Given that the liquid water response saturates near molecular resonances for fixed distance and distance response saturates for fixed water content, and the saturation brightness temperature shifts with the temperature of the atmosphere, rough determination of ambient temperature is also possible, especially if the local atmospheric transmission coefficient is known or can be estimated. The results suggest significantly larger responses than previous studies at 37 GHz and 89 GHz [4]; however, the non-cloud atmospheric conditions used in the present study may differ considerably from the previous work due to our choice of the Arctic domain.

The spectral flattening in the window region near the 183.31-GHz water vapor transition due to liquid clouds has been observed in preliminary experiments with horizontal-viewing G-band radiometers (Randolf Ware, private communications). While this suggests that the phenomenology is sound, additional simulations and observations of matching conditions are necessary for a full quantitative comparison between modeling and measurements. Future efforts look to incorporate cloud resolving model or observed cloud and precipitation data into the radiative transfer framework, as we have done in previous studies [28], [13], to investigate more representative atmospheric scenarios for forward-viewing sensors. Midlatitude systems that contain larger ice particles and snow aggregates with embedded liquid layers will be included to determine the effects of larger scatterers, as the impact of ice on the present simulations is minimal. Future simulations will also make use of refractive bending capabilities in ARTS.

Given the simulated responses, millimeter-wave, in particular G-band, sensors that will allow for reduced size and mass are feasible systems for detecting liquid clouds; however, the PCA suggests that additional information may be gained by including  $K_a$ -band radiometers when size, mass, and power constraints are less of a concern.

## REFERENCES

- [1] A.V. Matus and T.S. L'Ecuyer, "The role of cloud phase in earth's radiation budget," *J. Geophys. Res. Atmospheres*, vol. 122, no. 5, pp. 2559–2578, 2017, 2016JD025951.
- [2] A. Reehorst, D. Brinker, M. Politovich, D. Serke, C. Ryerson, A. Pazmany, and F. Solheim, "Progress towards the remote sensing of aircraft icing hazards," Tech. Rep. NASA/TM-2009-215828, National Aeronautics and Space Administration, November 2009.
- [3] W.J. Blackwell, "Radiometer development for small satellite microwave atmospheric remote sensing," in *2017 IEEE International Geoscience and Remote Sensing Symposium (IGARSS)*, July 2017, pp. 267–270.
- [4] G. G. Koenig, C. C. Ryerson, and J. A. Nagle, "Using RADTRAN to simulate an aircraft microwave radiometer to detect icing potential," in *42nd Aerospace Sciences Meeting and Exhibit*, 2004, pp. 141–144.
- [5] P. Eriksson, S.A. Buehler, C.P. Davis, C. Emde, and O. Lemke, "ARTS, the Atmospheric Radiative Transfer Simulator, version 2," *J. Quant. Spectrosc. Rad. Trans.*, vol. 112, pp. 1551 – 1558, 2011.

- [6] M. D. Shupe, J. S. Daniel, G. de Boer, E. W. Eloranta, P. Kollias, C. N. Long, E. P. Luke, D. D. Turner, and J. Verlinde, "A focus on mixed-phase clouds," *Bull. Amer. Meteor. Soc.*, vol. 89, pp. 1549–1562, Oct 2008.
- [7] K.G. Libbrecht, "The physics of snow crystals," *Reports on Progress in Physics*, vol. 68, no. 4, pp. 855, 2005.
- [8] G.P. Anderson, S.A. Clough, F.X. Kneizys, J.H. Chetwind, and E.P. Shettle, "Afgl atmospheric constituent profiles," Tech. Rep. AFGL-TR-86-0110, Air Force Geophysics Laboratory, May 1986.
- [9] Arnold Wexler, Richard Hyland, and Richard Stewart, *Thermodynamic properties of dry air, moist air and water and SI psychrometric charts*, ASHRAE, 1983.
- [10] M.D. Shupe, S.Y. Matrosov, and T. Uttal, "Arctic mixed-phase cloud properties derived from surface-based sensors at sheba," *Journal of the Atmospheric Sciences*, vol. 63, no. 2, pp. 697–711, 2006.
- [11] C. Davis, C. Emde, and R. Harwood, "A 3D polarized reverse Monte Carlo radiative transfer model for mm and sub-mm passive remote sensing in cloudy atmospheres," *IEEE Trans. Geosci. Remote Sens.*, vol. 43, pp. 1096–1101, May 2005.
- [12] D.L. Wu, J.H. Jiang, and C.P. Davis, "Eos mls cloud ice measurements and cloudy-sky radiative transfer model," *IEEE Trans. Geosci. Remote Sens.*, vol. 44, no. 5, pp. 1156–1165, May 2006.
- [13] I.S. Adams and M.H. Bettenhausen, "Brightness temperature simulation of observed precipitation using a three-dimensional radiative transfer model," *J. Atmos. Oceanic Tech.*, vol. 33, no. 10, pp. 2053–2064, 2016.
- [14] A. Battaglia, C.P. Davis, C. Emde, and C. Simmer, "Microwave radiative transfer intercomparison study for 3-d dichroic media," *J. Quant. Spectrosc. Rad. Trans.*, vol. 105, no. 1, pp. 55–67, 2007.
- [15] Michael I Mishchenko, "Calculation of the amplitude matrix for a nonspherical particle in fixed orientation," *Appl. Opt.*, vol. 39, pp. 1026–1031, Feb 2000.
- [16] C. Mätzler, "Dielectric properties of natural media: microwave dielectric properties of ice," in *Thermal Microwave Radiation: Applications for Remote Sensing*, C. Mätzler, Ed., pp. 455–463. The Institution of Engineering and Technology, 2006.
- [17] S. Giordano, "Effective medium theory for dispersions of dielectric ellipsoids," *Journal of Electrostatics*, vol. 58, no. 1, pp. 59 – 76, 2003.
- [18] Bruce T. Draine and Piotr J. Flatau, "Discrete-dipole approximation for scattering calculations," *J. Opt. Soc. Am. A*, vol. 11, no. 4, pp. 1491–1499, Apr 1994.
- [19] I. S. Adams and M. H. Bettenhausen, "The scattering properties of horizontally aligned snow crystals and crystal approximations at millimeter wavelengths," *Radio Sci.*, vol. 47, no. 5, pp. n/a–n/a, 2012, RS5007.
- [20] K.V. Mardia, *Statistics of Directional Data*, Academic Press, London, 1972.
- [21] Michael I Mishchenko and Larry D Travis, "Capabilities and limitations of a current FORTRAN implementation of the T-matrix method for randomly oriented, rotationally symmetric scatterers," *J. Quant. Spectrosc. Rad. Trans.*, vol. 60, pp. 309–324, Sep 1998.
- [22] D.D. Turner, S. Kneifel, and M. P. Cadeddu, "An improved liquid water absorption model at microwave frequencies for supercooled liquid water clouds," *J. Atmos. Oceanic Technol.*, vol. 33, pp. 33–44, Jan 2016.
- [23] P. W. Rosenkranz, "Absorption of microwaves by atmospheric gasses," in *Atmospheric Remote Sensing by Microwave Radiometry*, M A Janssen, Ed., pp. 37–90. Wiley, 1993.
- [24] P W Rosenkranz, "Water vapor microwave continuum absorption: A comparison of measurements and models," *Radio Sci.*, vol. 33, pp. 919–928, Apr 1998.
- [25] P W Rosenkranz, "Correction to 'water vapor microwave continuum absorption: A comparison of measurements and models'," *Radio Sci.*, vol. 34, pp. 1025, Apr 1999.
- [26] M. Yu. Tretyakov, M.A. Koshelev, V.V. Dorovskikh, D.S. Makarov, and P.W. Rosenkranz, "60-ghz oxygen band: precise broadening and central frequencies of fine-structure lines, absolute absorption profile at atmospheric pressure, and revision of mixing coefficients," *J. Molec. Spectrosc.*, vol. 231, pp. 1–14, May 2005.
- [27] L.S. Rothman, I.E. Gordon, Y. Babikov, A. Barbe, D. Chris Benner, P.F. Bernath, M. Birk, L. Bizzocchi, V. Boudon, L.R. Brown, A. Campargue, K. Chance, E.A. Cohen, L.H. Coudert, V.M. Devi, B.J. Drouin, A. Fayt, J.-M. Flaud, R.R. Gamache, J.J. Harrison, J.-M. Hartmann, C. Hill, J.T. Hodges, D. Jacquemart, A. Jolly, J. Lamouroux, R.J. Le Roy, G. Li, D.A. Long, O.M. Lyulin, C.J. Mackie, S.T. Massie, S. Mikhailenko, H.S.P. Mller, O.V. Naumenko, A.V. Nikitin, J. Orphal, V. Perevalov, A. Perrin, E.R. Polovtseva, C. Richard, M.A.H. Smith, E. Starikova, K. Sung, S. Tashkun, J. Tennyson, G.C. Toon, V.I.G. Tyuterev, and G. Wagner, "The hitran2012 molecular spectroscopic database," *Journal of Quantitative Spectroscopy and Radiative Transfer*, vol. 130, no. Supplement C, pp. 4 – 50, 2013.
- [28] I.S. Adams, P. Gaiser, and W. Linwood Jones, "Simulation of the stokes vector in inhomogeneous precipitation," *Radio Sci.*, vol. 43, no. 5, pp. n/a–n/a, 2008, RS5006.

**Ian S. Adams** (S'01-M'08) received the Ph.D. degree in electrical engineering from the University of Central Florida, Orlando, FL, USA in 2007.

From 2004–2006, he was a consultant with Microwave Remote Sensing Consultants, based in Cocoa Beach, FL. From 2006–2017, he was employed at the Naval Research Laboratory in Washington, DC, USA, where he studied the effects of precipitation on passive polarimetric remote sensing of ocean surface winds as well as vector radiative transfer of clouds and precipitation. He is currently a Research Physical Scientist with the Mesoscale Atmospheric Processes Laboratory at NASA Goddard Space Flight Center. His research interests include three-dimensional vector radiative transfer in precipitation, active and passive millimeter wave sensors, and geophysical forward model inversion.

Dr. Adams is a member of the American Geophysical Union and the American Meteorological Society. He served as vice-chair of the GRSS Frequency Allocation in Remote Sensing Technical Committee from 2010 to 2013.

**Justin Bobak** (M'89) received the Ph.D. degree in electrical engineering from The Pennsylvania State University, University Park, in 1998. His thesis work was on modeling the effects of turbulence on water vapor radiometer measurements.

He has over 20 years of experience in microwave radiometry, including hardware system design and retrieval algorithm development. He was Principal Investigator for the Airborne Polarimetric Microwave Imaging Radiometer (APMIR), an instrument designed and built at NRL to underfly SSMIS and WindSat. He worked on reflector coatings, calibration targets and error budgeting for NRLs MIS effort. He is the electrical lead for GLO, the GFCR solar Limb Occultation instrument. He has 26 publications and has earned two Berman Awards.

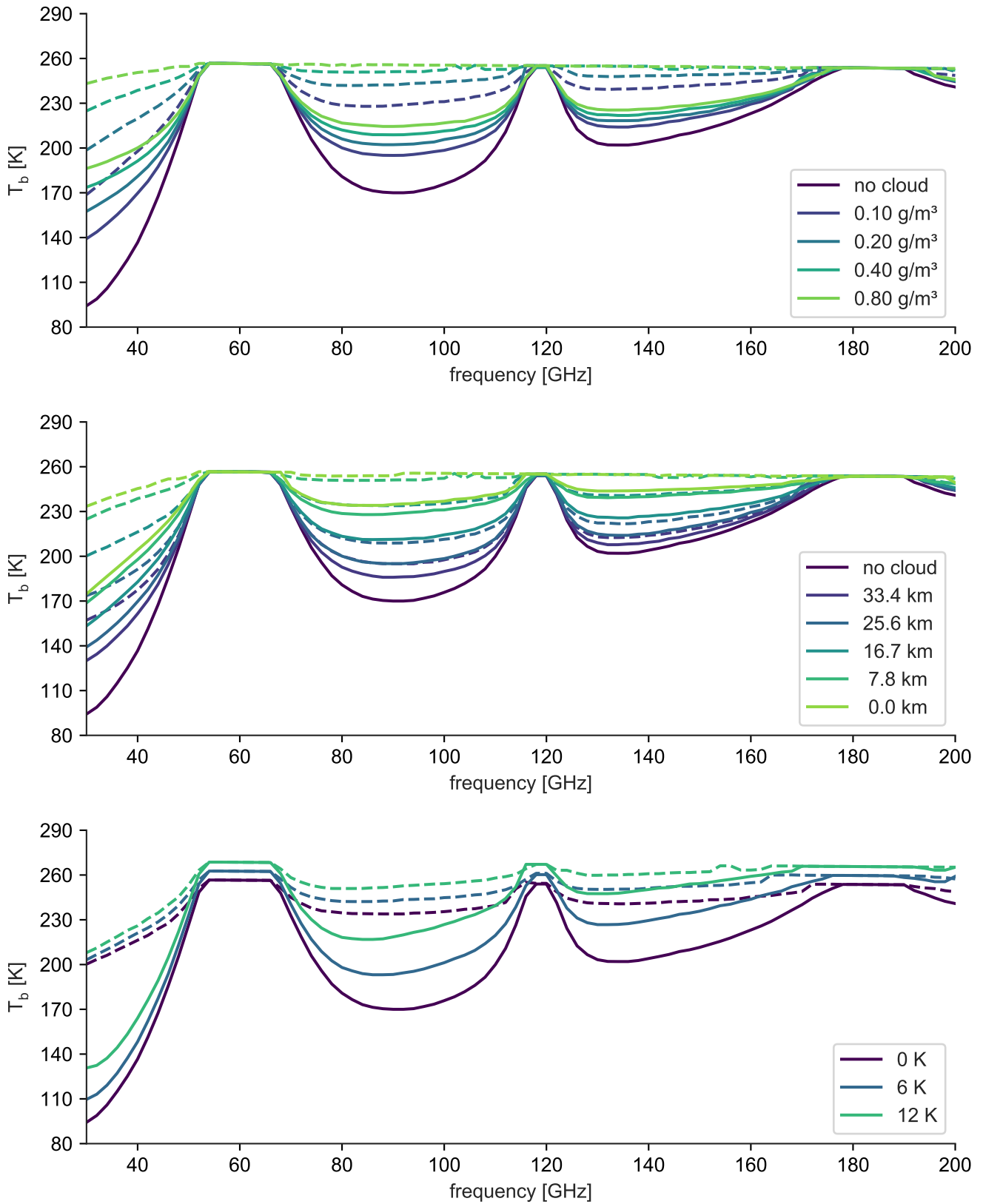


Fig. 3. Passive microwave  $T_b$  spectral dependence on liquid water content (LWC, top), range to cloud (middle), and temperature (bottom). When testing the dependence on liquid water content, the distance from the cloud edge was set to 25.6 km (solid) and 7.8 km (dashed). To demonstrate the dependence on cloud range, the LWC was fixed at 0.1 g m<sup>-3</sup> (solid) and 0.4 g m<sup>-3</sup> (dashed). When adding temperature shifts to the database temperature profile, the sensor was placed 16.7 km from the cloud edge for clear sky (solid) and LWC of 0.4 g m<sup>-3</sup> (dashed). For reference, the clear sky spectrum is also shown in the top and middle panels.

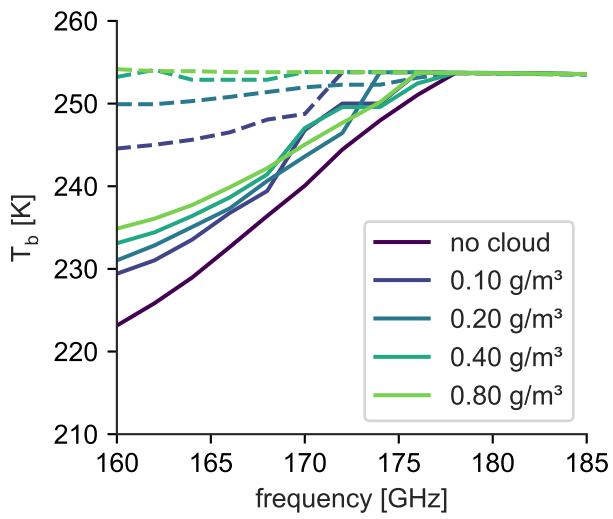


Fig. 4. Same as the top panel of Fig. 3, but with the axes limited to highlight the spectral response at G band near the 183.1 H<sub>2</sub>O absorption line.

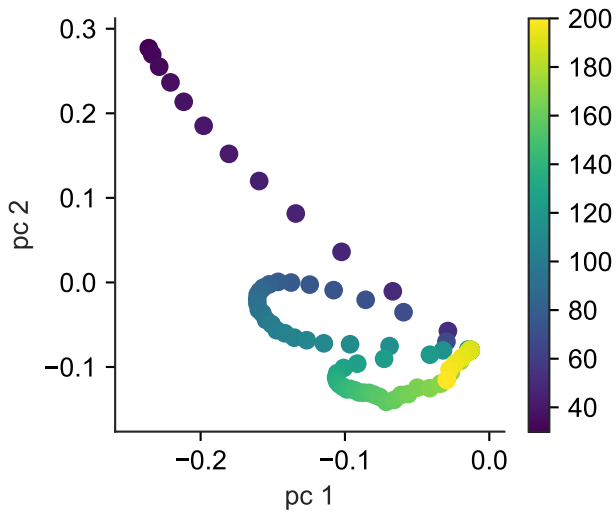


Fig. 5. First two principal components, colormapped to frequency.